

Comparative Analysis of Different UAV-Based Photogrammetric Processes to Improve Product Accuracies

Mirko Saponaro[1(✉)], Alessandra Capolupo[2], Eufemia Tarantino[1], and Umberto Fratino[1]

[1] Politecnico di Bari, via Orabona 4, 70125 Bari, Italy
mirko.saponaro@poliba.it
[2] Plinivs Research Center – LUPT, University of Naples Federico II, Via Toledo, 402, 80134 Naples, NA, Italy

Abstract. Producing geographic information has become increasingly widespread over the last few years thanks to the development of new sensors, tools and algorithms, easily to be implemented and user friendly. Nevertheless, the accuracy of photogrammetric outcomes, obtained by automated software instructions and the use of un-calibrated cheap sensors, is often unsatisfying. As a consequence, the results accuracy and the potentialities and repeatability of those procedures have to be improved, defining the best workflow to be adopted. In literature, different approaches related to the correct and efficient reduction of geometric errors are available, although, to date, comprehensive method has not yet been defined.

This research work is aimed to detect an optimized workflow on the base of the comparison the accuracies achieved by applying different 3D reconstruction procedures of the cultural heritage. The process was subdivided in two steps: the former is related to a processing test, executed by analyzing four image-datasets acquired with a prosumer UAV equipped with a non-metric camera and a low-accuracy GNSS/INS receiver; the latter is based on an high-accuracy ground-truth survey, performed to evaluate the lever-arm and the camera self-calibration parameters, which are fundamental for reducing the errors propagation in the final accuracy. Thus, different 3D models were generated, modifying the processed image datasets and the spatial and numerical distribution of the Ground Control Points (GCPs). The root-mean-square error (RMSE) values on the Control Points (CPs), compensated differently in the Bundle Block Adjustment process, were assessed for each processing. Promising results were achieved in order to validate an optimal photogrammetric workflow.

Keywords: UAV · Direct Georeferencing · Lever-arm · Self-calibration

1 Introduction

The technological advances of sensors and algorithms and the introduction of new tools, such as Unmanned Aerial Vehicles (UAVs), in the field of survey have strongly improved the outcomes accuracy produced by photogrammetric technique.

© Springer Nature Switzerland AG 2019
S. Misra et al. (Eds.): ICCSA 2019, LNCS 11622, pp. 225–238, 2019.
https://doi.org/10.1007/978-3-030-24305-0_18

The combination of UAVs ability to overflow areas hard to access and to reduce operational time and cost with the improvements to Structure from Motion (SfM) and Multi-View Stereo (MVS) algorithms making photogrammetry more competitive than the traditional survey systems on the small and medium-sized areas [1]. Nevertheless, James et al. [2] highlighted that a homogeneous quality of the outcomes is still tough to reach and, therefore, as proposed by Manfreda et al. [1], the whole workflow should be subjected to a critical inspection for detecting the best approach among the several possible methods. Although, in literature, there are traces of procedures to be adopted for reducing correctly and efficiently the geometric errors, an exhaustive method has not yet been validated [3, 4].

Currently, the most widespread UAVs are equipped with L1 single-frequency and/or C/A code GNSS receivers, assisted with low-cost Inertial Measurement Unit (IMU) and non-metric cameras. Consequently, that low-equipment is not able to guarantee the achievement of standard accuracy requirements. This is complicated by the lack of information on the used processing algorithms and the clear definition of the relationships among parameters. Indeed, for instance, most of the available SfM software operate as a black-box, in which several parameters are preset [5] or, as in the case of the environments chosen to calibrate the camera mounted on UAVs, discussed in several papers [2, 6]. That last step is essential since camera lenses often introduce significant non-linear geometric distortions into the images, compromising their overall accuracy. Therefore, it is generally concerted that, unless an accurate pre-calibration is performed onsite, a robust self-calibration procedure is indispensable in order to compensate the inherent instability of the consumer cameras mounted on-board [7]. Thus, the synchronization between camera and navigation system, the determination of the exposure time of each image and, above all, of the lever-arm offset between the Perspective Center (PC) camera position and the GNSS Antenna Phase Center (APC) are required [8]. This constant displacement vector is rarely introduced in the processing software to compensate the lever-arm offset, affecting the final accuracy.

Apart from the camera, the on-board GNSS receiver is the other crucial tool mounted on the UAV. It is essential both for planning and driving the aircraft, and Direct Georeferencing (DG) of images during the SfM processing. The DG is a crucial step towards the automating all the procedure, however, as demonstrated in several papers [6, 9–11], their results are not satisfactory results compared to Indirect Georeferencing (IG). For that reason, the topographic UAV-based processing is generally performed using some known points, defined Ground Control Points (GCPs). The output accuracy of that method depends on the number and accuracy of GCPs involved in the metric reconstruction. Clearly, operational cost and time increase proportionally to the GCPs acquired during the field campaigns [12, 13], and, consequently, optimizing the survey activities would hence improve the reliability and repeatability of UAV-derived products [5].

The present work is aimed to define the best workflow in order to maximize the accuracy of the photogrammetric outcomes, comparing some 3D models of cultural heritage produced applying several approaches. Basic processing methods was screened to identify the most effective strategy for a reliable evaluation of camera calibration and lever-arm offset. Then a scheme of systematic errors related to the number of GCPs used and their spatial distribution was constructed.

2 Material and Method

A comprehensive UAV-based photogrammetric workflow was tested in order to improve the interior and exterior orientation parameters, and to reduce the error during computing process.

The process was split in two steps. The former based on the analysis of four images datasets acquired by applying a prosumer UAV equipped with a non-metric camera and a low-accuracy GNSS/INS receiver. The density of the obtained points clouds was gradually reduced, by selecting the points on the base of three cleaning criteria, described more in depth in the following paragraphs. The latter, based on an high-accuracy ground-truth survey, was carried out to evaluate the lever-arm and the camera self-calibration parameters. Particularly, the error must be mathematically modelled since these lens distortions and displacement vector are systematic effects.

The last phase is aimed to pull out on different 3D models. Combining the effects of image datasets with GCPs spatial and numerical distribution, systematic errors and the accuracy variation, reported as the root-mean-square-error (RMSE), on the Control Points (CPs), compensated differently in the relative phase of the Bundle Block Adjustment (BA), were then assessed.

2.1 Study Area, Data and Technology

The experiment was carried out in a farmhouse called 'Casale di Pacciano', located in the countryside of Bisceglie, 40 km far away from Bari (Puglia Region, Southern Italy). The farmhouse, dated back to the 11th century (Fig. 1), was already examined by the Polytechnic University of Bari in previous work [14].



Fig. 1. The test site and GCPs distributed in the area

It was over flown during two flight campaigns, performed using a prosumer quadcopter DJI Inspire 1, programmed through the iOS app DJI Ground Station Pro. The UAV was equipped with a non-metric camera DJI ZenMuse X3, characterized by a focal length of 3.61 mm and a pixel size of 1.56 μm. Moreover, it was also equipped with an economical GNSS/INS receiver, which the average accuracy of 2.54 m along the axes.

The two missions were planned in order to acquire images converging two opposite sides of the building. The former was managed at the constant altitude of 30 m Above Ground Level (AGL) in order to obtain an Average Ground Sample Distance (GSD) equal to 0.013 m/pix. The camera was set in a nadir-position. The latter was performed at a altitude of 20 m AGL, inclining the camera at 45°. In this case a GSD equal to 0.009 m/pix was expected. The image overlap was set to 90% in both longitudinal and lateral direction of the flight.

Three datasets were generated (Table 1): the "NAD" dataset composed only by nadiral images; the "NAD+45°" source of data consisted by all the images acquired during the two missions; the "NAD+CON" dataset characterized by 11 selected convergent images taken during the second flight. UAV flights patterns with different heights and additional cross strip introduce additional depth information and support efficient calibration of low-cost cameras [3].

Table 1. Imagery dataset features

Dataset	n° images	Camera inclination	Altitude AGL [m]	GSD [m/pix]	Image size	Pixel size [μm]	Focal length [mm]	Image quality
NAD	75	90°	30	0.013	4000 × 3000	1.56	3.61	0.8528
NAD+CON	86	90°/45°	30/20	0.013/0.009	4000 × 3000	1.56	3.61	0.8525
NAD+45°	194	90°/45°	30/20	0.013/0.009	4000 × 3000	1.56	3.61	0.8515

Each acquired image was correlated with the information related to their position on the moment of shooting.

The metric reconstruction was improved using 8 GCPs, homogeneously distributed along the border and the central side of the study area (Fig. 1). Their coordinates were accurately detected through the application of the Global Navigation Satellite System (GNSS) Leica Viva GS14 receivers, performing measurements in Real Time Kinematic (RTK) relying on a baseline between the static master station and the "Margherita di Savoia" permanent reference station of the National Dynamic Network (RDN2008). Their features are described in Table 2. The metric reconstruction was implemented in Agisoft PhotoScan environment (version 1.4.1).

2.2 Workspace Setting and Calibration System

A reasonable calibration of the system and a workspace setting was fixed. The quality of images was checked in order to detect and remove images, not suitable for the photogrammetric processing purposes. PhotoScan software provides a useful tool that independently analyses each image, estimating for it a quality value between 0 (low) and 1 (high). Table 1 shows the average values of the image quality, which are

Table 2. GCP coordinates features

GCP label	Easting [m]	Northing [m]	Geodetic height [m]	Accuracy E [m]	Accuracy N [m]	Accuracy H [m]
GNSS001	623202.809	4563587.783	68.551	0.001825	0.001714	0.008375
GNSS002	623227.598	4563583.821	66.682	0.004196	0.003988	0.019079
GNSS003	623220.777	4563599.963	66.107	0.004158	0.003709	0.017090
GNSS004	623216.743	4563605.399	66.104	0.004167	0.003744	0.016646
GNSS005	623235.381	4563588.782	67.835	0.004266	0.003889	0.017085
GNSS006	623233.660	4563606.238	65.799	0.004588	0.004079	0.016514
GNSS008	623239.901	4563582.427	67.771	0.004447	0.004246	0.013493
GNSS011	623260.574	4563621.193	65.373	0.004414	0.004113	0.012621

higher than the threshold 0.5, and, consequently, no of them should be removed. Moreover, the images didn't show any evident distortions or blur effects.

The reference system WGS84 (EPSG::4326) was defined for the imagery qualified by the geo-tags, while for the detected GCPs the reference system RDN2008/UTM zone 33N (NE) (EPSG::6708) was set. In Accuracy Image (m) parameter a value of 3 m was chosen as conservative setting, although knowing the actual value equal to 2.54 m. The precision of this value is linked to the receiver rate of position measurements per second (Hz) and accordingly to the mean speed of the aircraft [8]. However, despite the imagery are acquired in hovering and the precision can be considered robust, a conservative value is recommended. At the same time, since there are no manufacturing information, in Accuracy Image (deg) the default value of 10° is retained, so as to incorporate within it the negative effects caused by the low accuracy of the IMU-onboard. The Precision Marker (m) parameter was set a mean value of 0.02 m: that parameter represents the mean precision of GCPs coordinates in object space. As regards the calibration of the image coordinates in the software workspace, a more realistic Marker Precision (pix) value of 0.5 pix was set, i.e. the actual ability of the operator to identify the target in the image. The accuracy of the tie points is kept at the default value of 1 pix [3]. The images sharpness influences the tie points positioning. A subpixel value of this parameter prevents the photogrammetric block from being distorted, but at the same time it cut the points re-projections number. The Tie points accuracy, Precision Marker (pix) and Precision Marker (m) parameters are used to construct the variance-covariance matrix within the stochastic model, thus primary for the BA optimization.

An additional dataset characterized by the union of the nadiral image dataset with the calibration file, named NAD+CALIBR, was generated using the Agisoft Lens tool in the laboratory. The camera calibration of the other datasets was obtained during the cameras alignment step.

It is important to set the GPS/INS Offset in order to obtain the lever-arm values corrections measured in the laboratory. Precisely, the displacement vector (X, Y, Z) measured is equal to (0.005, 0.10, 0.25) m with precision of about 0.01 m, and IMU values calibration (yaw, pitch, roll) is put equal to 0° with an accuracy equal to 2°. These values were optimized in the consecutive phases.

Once the workspace was set up, the Camera Alignment step was run with 'high' accuracy option, setting the Limit of Key Points and Tie Points equal to 0. Once the cameras alignment the of all processes was completed and interior and exterior orientation and camera calibration parameters were defined, the cleaning clouds process started by utilizing three picking criteria of the Gradual Selection tool [3]. The first criterion utilized, named Reconstruction Uncertainty, allows removing points with low base-to-height ratios. Namely, tie points situated in the margins of the surveyed area generally have a higher degree of reconstruction uncertainty than those in the model centre, due to the low lateral overlapping of the images. Removal of such points don't affect the accuracy of optimization, but beneficially lightens the model.

The second criterion utilized, called Projection Accuracy, allows identifying less reliable tie points. In this work case, poor quality matches are indicated by a parameter value equal to 10 which means, that those points have an uncertainty 10 times higher than the points of minimum uncertainty.

The third criterion, the Re-projection Error, is applied to remove erroneous points with big residuals. Effectively, this parameter involves the largest direct influence on the root-mean-square-error (RMSE) of the GCPs and CPs, and it improve conspicuously the orientation parameters.

As suggested by Mayer et al. [3], the obtained points cloud was subjected to a Gradual Selection treatment, as reported in Table 3. The clouds are cleaned out from inaccurate points for the accuracy optimization, whereupon 8 GCPs are identified in the images.

Table 3. n° of tie points reduction in Gradual Selection processes in 1st step

Dataset	Initial n° tie points	Reconstruction Uncertainty [Value 10]	Projection Accuracy [Value 3]	Reprojection Error [Value 0.40]
NAD	282202 →	147874 →	101343 →	88538
NAD+CON	319609 →	152800 →	104516 →	93021
NAD+45°	741240 →	228767 →	161548 →	142373
NAD +CALIBR	292000 →	155994 →	105777 →	68491

The Bundle Block Adjustment (BA) procedures were launched through the Optimize Cameras process, which were used to adjust the coordinates of estimated points, camera parameters and lever-arm values minimizing the sum of re-projection errors and reference coordinate misalignment error [3]. Nevertheless, it is able to compensate only the linear model misalignment, and not the non-linear components.

The applied operations yielded estimates of the calibration parameters of the camera and of the lever-arm vector for each processed dataset.

2.3 3D Model Generation Workflow

Subsequently, the datasets were carried out using three Chunks. The alignment of cameras in 'high' precision mode was started, in order to generate the three sparse points clouds. The procedure applied was equal to that one described in the first step, the clouds were treated in Gradual Selection, reducing the size and re-projection errors related to the uncertainty and ambiguity of the points (Table 4).

Table 4. n° of tie points reduction in Gradual Selection processes in 2nd step

Dataset	Initial n° tie points	Reconstruction Uncertainty [Value 10]	Projection Accuracy [Value 3]	Reprojection Error [Value 0.40]
NAD	281896 →	147477 →	101040 →	88107
NAD+CON	319456 →	152718 →	104337 →	92670
NAD+45°	741274 →	228569 →	161429 →	142086

In order to understand the influence of the number of GCPs used and their spatial distribution for the optimization of the accuracy of the UAV-based products, the 8 GCPs reported in Table 2 and Fig. 1 were again introduced in the three Chunks.

Number of GCPs. Nine copies were generated for each Chunk, in a total of 27 sparse points cloud in the workspace. The nine clouds for Chunk have been georeferenced by implementing from a maximum of 8 GCPs to 0 GCPs, thus considering also the case of DG. The implemented GCPs were chosen according to the common criterion which start from the more external points up to the more central ones of the reconstructed 3D model [3]. The remaining number of non-implemented ground points in each process are consequently defined as CPs.

Once the casuistry was defined, the BA was run applying the Optimize Cameras process, which it is strictly conditioned by the fixed georeferencing.

GCPs Spatial Distribution. Starting from the three basic Chunks, for each of these, additional copies were generated: the influence of the spatial distribution of GCPs varies according to the number of those implemented [12]. At the beginning, 7 clouds of points were generated for each Chunk, with a number of GCPs ranging from 1 to 7, adopting an opposite strategy of choice than the previous case, i.e. from central GCPs to those on borderlines. Further for each Chunk, other 7 clouds have been generated but adopting another GCPs strategy of choosing, i.e. balancing homogeneously the distribution. The workspaces were organized with a total of 42 Chunk: the Optimize Cameras procedure was started.

3 Results and Discussion

3.1 Camera Calibration and Lever-Arm

Figure 2 shows the differences among the different calibrations estimated in the four processes described in Sect. 2.2. In particular, Fig. 2a reports the differences of trends among the estimated values in the different processes for each parameter. In order to make indicative the representation, the value of the focal length F was set as the percentage of the difference from the initial theoretical value, while the other parameters were represented using their actual estimated values. The figure shows that there are no substantial differences among the estimates since their trends are analogous. The outcomes obtained from the Chunks NAD+45° and NAD+CON reveal a similar behaviour, pointing out the opportunity to reduce the acquisition and processing time. The comparison of the Standard Deviation (SD) values, resulting from each parameter estimation, is reported in Fig. 2b. The SDs of the NAD+45° dataset (the blue lines) show a more robust results compared to the others. The values regarding the Chunk NAD+CALIBR are not reported in the figure since they are identified as outliers because of their non-conforming values. This demonstrated that the pre-calibration procedure performed in the laboratory has low reliability.

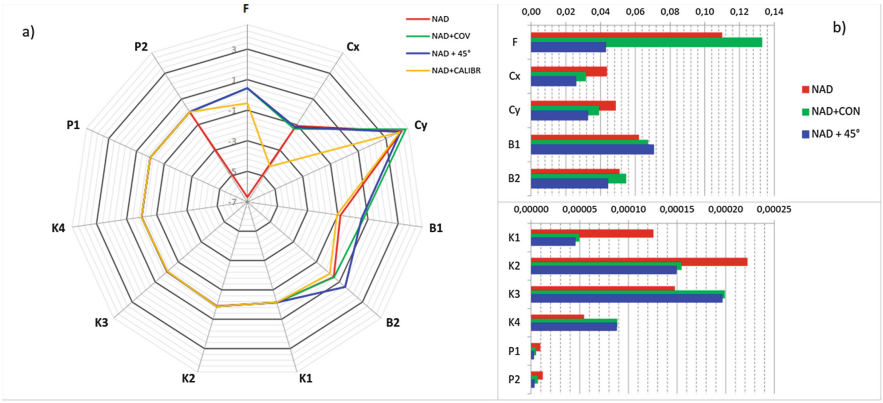

Fig. 2. (a) Graphical comparison of camera calibration parameters. In F that mean the focal length, the value represents a percentage difference from the initial theoretical value. Cx and Cy describe the offset of the main point. K1-K2-K3-K4 are related to the radial distortion coefficients while P1 and P2 to the tangential distortion coefficients. The B1-B2 parameters mean the affinity value and the non-orthogonality coefficient. (b) SD values resulting from the computing

In order to identify the most suitable processing for extracting the optimal values of the camera calibration parameters, the variance-covariance matrices have been extrapolated (Fig. 3). Comparing the covariances among the Chunks, a percentage reduction of the correlation in the Chunk NAD+45° is traced. Covariance is an reliable index to estimate camera calibration since its reduction indicates the estimation errors

of each parameter are independence. Like in the previous case, the NAD+CON model shows results that are directly comparable with the previous one. Therefore, the parameters estimated in NAD+45° are selected.

Once defined camera calibration parameters, the values of the lever-arm were detected in order to mitigate the interior and relative exterior orientation errors of the cameras. Although the values of lever-arm appear comparable, except for the Chunk NAD+CALIBR because of the high RMSE of GCPs, as shown in Fig. 4, the lever-arm parameters obtained from NAD model were chosen, since the other Chunks were characterized by a higher re-projection errors (pix).

NAD	F	Cx	Cy	B1	B2	K1	K2	K3	K4	P1	P2
F	1	0.04	0.03	0.05	0.01	0.92	0.88	0.59	0.55	0.02	0.1
Cx		1	0.04	0.06	0.03	0.03	0.03	0.02	0.02	0.67	0.09
Cy			1	0.09	0.13	0.06	0.03	0.02	0.01	0.07	0.62
B1				1	0.05	0.08	0.05	0	0.01	0.13	0.13
B2					1	0	0.01	0.01	0.02	0.01	0.16
K1						1	0.95	0.77	0.71	0	0.11
K2							1	0.9	0.86	0	0.1
K3			symm.					1	0.99	0.02	0.07
K4									1	0.01	0.06
P1										1	0.18
P2											1

NAD+CON	F	Cx	Cy	B1	B2	K1	K2	K3	K4	P1	P2
F	1	0.02	0.2	0.14	0.04	0.09	0.23	0.12	0.13	0.05	0.19
Cx		1	0.03	0.01	0.09	0.03	0.01	0.02	0.03	0.12	0.02
Cy			1	0.03	0.02	0.01	0.04	0.01	0.02	0.01	0.21
B1				1	0.07	0.07	0.02	0.05	0.06	0.09	0.1
B2					1	0.01	0.01	0.01	0.01	0.09	0.03
K1						1	0.9	0.86	0.79	0.06	0.07
K2							1	0.98	0.95	0	0.04
K3			symm.					1	0.99	0.01	0.02
K4									1	0.01	0.02
P1										1	0.13
P2											1

NAD+45°	F	Cx	Cy	B1	B2	K1	K2	K3	K4	P1	P2
F	1	0.01	0.2	0.15	0.11	0.16	0.22	0.19	0.18	0.05	0.07
Cx		1	0.09	0.03	0.33	0.01	0	0.01	0.02	0.53	0.06
Cy			1	0.03	0.02	0.02	0.02	0.02	0.02	0.05	0.49
B1				1	0.03	0.08	0.01	0.04	0.05	0.05	0
B2					1	0	0.01	0	0.01	0.12	0.03
K1						1	0.96	0.9	0.85	0	0.08
K2							1	0.98	0.95	0.02	0.03
K3			symm.					1	0.99	0.02	0.02
K4									1	0.02	0.01
P1										1	0.02
P2											1

Fig. 3. Variance-Covariance matrices extrapolated from the Calibration Camera stochastic models of each processing. Values between 0 and ±1 that indicate relatively no-correlation or full correlation.

GPS/INS Offset – *Lever-Arm*

NAD	*Initial [m]*	*Adjusted [m]*	*Accuracy [m]*
X [m]	0.0050	0.0023	0.0100
Y [m]	0.1000	0.0998	0.0100
Z [m]	0.2500	0.2505	0.0100
Yaw [°]	0	0.8377	2
Pitch [°]	0	5.7062	2
Roll [°]	0	1.7367	2

NAD+CON	*Initial [m]*	*Adjusted [m]*	*Accuracy [m]*
X [m]	0.0050	0.0022	0.0100
Y [m]	0.1000	0.0998	0.0100
Z [m]	0.2500	0.2487	0.0100
Yaw [°]	0	0.5442	2
Pitch [°]	0	0.7121	2
Roll [°]	0	1.3552	2

NAD+45°	*Initial [m]*	*Adjusted [m]*	*Accuracy [m]*
X [m]	0.0050	0.0027	0.0100
Y [m]	0.1000	0.0994	0.0100
Z [m]	0.2500	0.2485	0.0100
Yaw [°]	0	0.2391	2
Pitch [°]	0	-21.3456	2
Roll [°]	0	0.7601	2

NAD+CALIBR	*Initial [m]*	*Adjusted [m]*	*Accuracy [m]*
X [m]	0.0050	0.0023	0.0100
Y [m]	0.1000	0.0997	0.0100
Z [m]	0.2500	0.2490	0.0100
Yaw [°]	0	0.8182	2
Pitch [°]	0	5.8299	2
Roll [°]	0	1.7480	2

Fig. 4. In the first table are presented the comparable RMSE values about the 4 Chunk. At the second table the different estimated GPS/INS Offsets extrapolated from PhotoScan.

3.2 Positional Accuracy Assessment

Number of GCPs Impact. Table 5 shows the RMSE values related to the 27 datasets processing, obtained varying the number of GCPs used in the BA procedures and, consequently, in georeference phase. The RMSE values define the overall trend of systematic errors recorded in the GCPs and in the remaining CPs along the three axes. 8 and 0 GCPs were used in the IG and DG procedure, respectively. As described in Sect. 2.1, the low accuracy of the sensors mounted on board the UAV does not allow the achievement of high positional accuracy in the DG. DG procedure shows important deviations along the Y axis. This highlighted the lack of reliability of the data recorded by the on-board receiver. The lack of raw position data acquired by the on board receiver does not allow, however, to investigate the causes and, thus, their estimation cannot be improved. In order to go beyond this problem, It is necessary to include an efficient amount of GCPs in the data processing workflow in order to increase the accuracy of geospatial products.

Overall, the three datasets show a similar behavior respect to the number of GCPs implemented. There is a reduction in RMSE values in the transition from a number of GCPs used from 2 to 3, with a RMSE value of 5.7 cm in the NAD+CON dataset. The following steps confirm the order of magnitude achieved with slight centimetric improvements. By focusing on the differences between the three processed datasets, some considerations emerge. The NAD+45° dataset returns a better RMSE value by implementing only one GCP. The subsequent values reveal a worsening of the estimates compared to the other datasets due to the relative increase in the errors of re-projection of the points. A rather similar trend is recorded on the NAD and NAD+CON datasets until the implemented of 6 GCPs. Beyond that limit, NAD+CON is affected by the points' re-projection errors equally to NAD+45°. The value of absolute geometric accuracy achieved by NAD with 7 GCPs implemented is comparable to the value of GSD, defined in Sect. 2.1.

Table 5. RMSE values achieved by varying the number of GCPs implemented

	n° GCPs	RMSE [NAD]				RMSE [NAD+CON]				RMSE [NAD+45°]			
		X (m)	Y (m)	Z (m)	XYZ (m)	X (m)	Y (m)	Z (m)	XYZ (m)	X (m)	Y (m)	Z (m)	XYZ (m)
GCP	0	–	–	–	–	–	–	–	–	–	–	–	–
CP		1.053	3.372	1.532	3.8500	1.373	3.406	1.310	3.8995	1.846	3.140	1.202	3,8358
GCP	1	0.000	0.000	0.000	0.0003	0.000	0.000	0.000	0.0004	0.000	0.000	0.001	0.0012
CP		0.519	0.428	1.759	1.8830	0.494	0.648	1.530	1.7332	0.511	1.387	0.907	1.7337
GCP	2	0.007	0.013	0.021	0.0254	0.000	0.000	0.002	0.0020	0.000	0.000	0.003	0.0026
CP		0.054	0.073	0.803	0.8084	0.032	0.074	0.830	0.8339	0.056	0.126	0.926	0.9366
GCP	3	0.012	0.028	0.033	0.0450	0.006	0.005	0.010	0.0127	0.007	0.013	0.003	0.0150
CP		0.024	0.017	0.064	0.0706	0.022	0.025	0.046	0.0570	0.057	0.069	0.073	0.1154
GCP	4	0.013	0.020	0.064	0.0688	0.018	0.015	0.036	0.0428	0.018	0.012	0.058	0.0616
CP		0.025	0.019	0.039	0.0495	0.023	0.031	0.019	0.0426	0.057	0.079	0.030	0.1020
GCP	5	0.012	0.017	0.058	0.0613	0.017	0.013	0.035	0.0408	0.019	0.011	0.052	0.0566
CP		0.030	0.021	0.040	0.0545	0.027	0.035	0.015	0.0471	0.063	0.092	0.033	0.1157
GCP	6	0.019	0.019	0.059	0.0651	0.019	0.012	0.030	0.0378	0.047	0.050	0.051	0.0858
CP		0.023	0.016	0.002	0.0276	0.017	0.041	0.016	0.0467	0.030	0.048	0.011	0.0575
GCP	7	0.023	0.019	0.055	0.0622	0.019	0.021	0.033	0.0430	0.044	0.052	0.047	0.0825
CP		0.009	0.007	0.005	0.0123	0.010	0.008	0.027	0.0298	0.002	0.002	0.020	0.0205
GCP	8	0.021	0.017	0.051	0.0581	0.018	0.019	0.031	0.0410	0.041	0.048	0.044	0.0771
CP		–	–	–	–	–	–	–	–	–	–	–	–

GCPs Spatial Distribution Impact. The spatial location of the GCPs on the image block was also taken into account. Figure 5a shows the interpolated trend lines by examining the RMSE values of the CPs obtained from the three GCPs spatial configurations, in response to changes in their number. The trend lines, concerning the RMSE variations of GCP points, are also shown in order to obtain a complete overview of the geometric accuracy achieved in each model. Trend lines mitigate the effects of the different spatial distribution of points, defining a general trend in accuracy. Overall, the trends of the values of CPs confirm the previous results even if, they show some appreciable improvements for the NAD+CON and NAD+45° datasets. This means that a different spatial distribution of the implemented GCPs affects re-projection errors and the achievable accuracy. On the other hand, a compensation of about 2–4 cm of the errors of the GCPs, in the NAD+CON modelling, represent a reasonable correctness of the internal and external orientation of the model. Finally, Figs. 5b–c–d show the statistical treatment for each model, so as to examine the best distribution strategy of GCPs. The third selected spatial distribution returns better accuracy values. In particular, as discussed by Rangel et al. [12], the best results are obtained with a gradual GCPs distribution in order to obtain a homogeneous density of the points in the area, maintaining a reasonable distance among the points. Promising results are also generated from the first spatial distribution, including marginal GCPs and central CPs, according to the literature [12, 13].

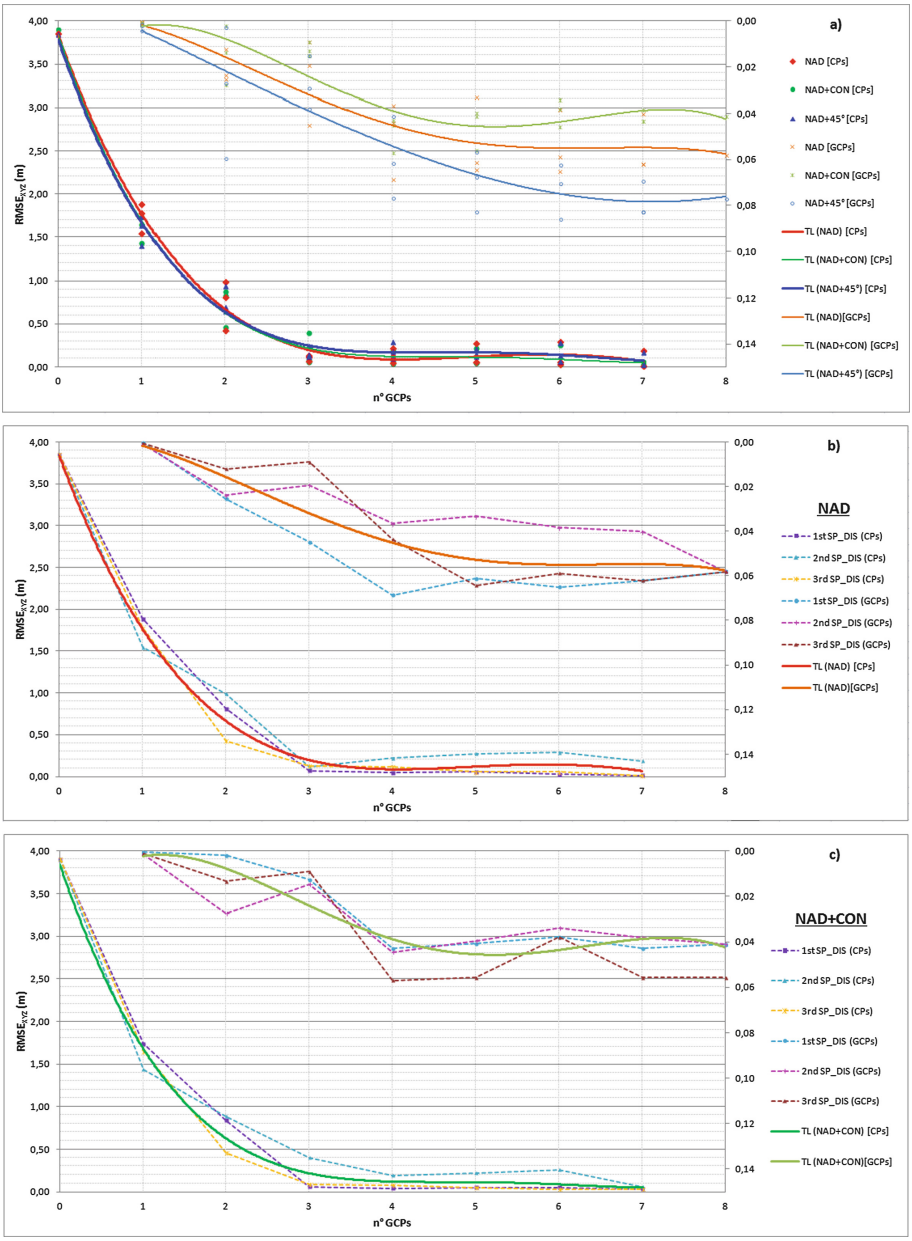

Fig. 5. Impact of GCPs spatial distribution. (a) Trend lines interpolated on 3 different spatial distributions of GCPs by varying the number of these latter. (b) NAD dataset developments and trend line by varying the spatial distribution. (c) NAD+CON dataset developments and trend line by varying the spatial distribution. (d) NAD+45° dataset developments and trend line by varying the spatial distribution.

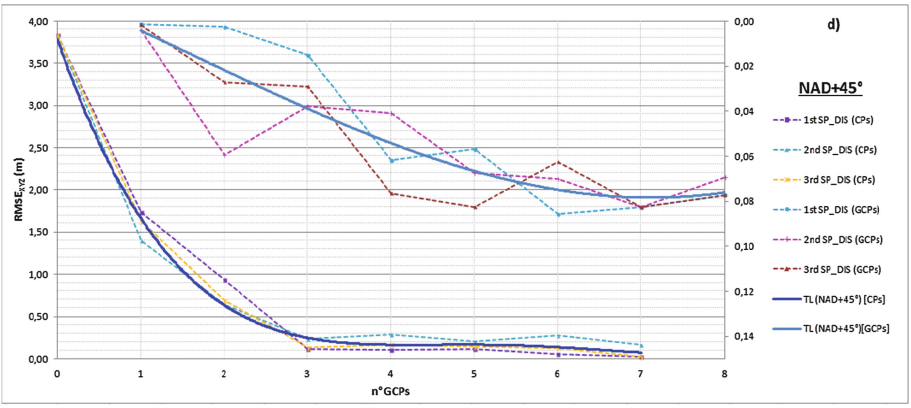

Fig. 5. (*continued*)

4 Conclusion

The current research activity is aimed to identify the most effective comprehensive workflow to increase the accuracy of the photogrammetric outcomes as much as possible. Therefore, this work demonstrated that a reliable camera calibration and lever-arm vector estimation avoid errors propagation in the final product accuracy and its repeatability. Moreover, UAV flights performed at different heights, camera inclinations and additional cross strip introduce additional depth information and support efficient calibration of low-cost cameras. Sparse points clouds obtained have to be treated identifying tie points with low-quality matching and high re-projection errors, and therefore removed prior to BA process. Subsequently, the influence of the final accuracy of the number and spatial distribution of the GCPs was detected. In the meanwhile, appreciable differences in accuracy were investigated by examining combined image datasets.

Results generated by the dataset of nadiral images, assisted only by 11 convergent images, look interesting. Obvious gaps were highlighted about the DG, noting instead the need of only 3 GCPs for a high quality geo-referencing. Moreover, homogeneous distribution of GCPs improves the metric reconstruction accuracy.

Future applications should be aimed to make more efficient the photogrammetric processing. A possible future application will automate the research of the optimal spatial and numerical distribution of the GCPs.

References

1. Manfreda, S., et al.: On the use of unmanned aerial systems for environmental monitoring. Remote Sens. **10**, 641 (2018)
2. James, M.R., Robson, S., d'Oleire-Oltmanns, S., Niethammer, U.: Optimising UAV topographic surveys processed with structure-from-motion: ground control quality, quantity and bundle adjustment. Geomorphology **280**, 51–66 (2017)

3. Mayer, C., Gomes Pereira, L., Kersten, T.P.: A comprehensive workflow to process UAV images for the efficient production of accurate geo-information. In: IX National Conference on Cartography and Geodesy (2018)
4. Saponaro, M., Tarantino, E., Fratino, U.: Geometric accuracy evaluation of geospatial data using low-cost sensors on small UAVs. In: Gervasi, O., et al. (eds.) ICCSA 2018. LNCS, vol. 10964, pp. 364–374. Springer, Cham (2018). https://doi.org/10.1007/978-3-319-95174-4_29
5. Manfreda, S., et al.: Accuracy assessment on unmanned aerial system derived digital surface models. Preprints.org (2018)
6. Gabrlik, P., Cour-Harbo, A.l., Kalvodova, P., Zalud, L., Janata, P.: Calibration and accuracy assessment in a direct georeferencing system for UAS photogrammetry. Int. J. Remote Sens. **39**, 4931–4959 (2018)
7. Benassi, F., et al.: Testing accuracy and repeatability of UAV blocks oriented with GNSS-supported aerial triangulation. Remote Sens. **9**, 172 (2017)
8. Padró, J.-C., Muñoz, F.-J., Planas, J., Pons, X.: Comparison of four UAV georeferencing methods for environmental monitoring purposes focusing on the combined use with airborne and satellite remote sensing platforms. Int. J. Appl. Earth Obs. Geoinf. **75**, 130–140 (2019)
9. Daakir, M., et al.: Lightweight UAV with on-board photogrammetry and single-frequency GPS positioning for metrology applications. ISPRS J. Photogram. Remote Sens. **127**, 115–126 (2017)
10. Grayson, B., Penna, N.T., Mills, J.P., Grant, D.S.: GPS precise point positioning for UAV photogrammetry. Photogram. Rec. **33**, 427–447 (2018)
11. Hu, J., et al.: A brief review on the positioning technologies for unmanned aerial vehicles. In: IEEE International Conference on Unmanned Systems (ICUS), pp. 527–532 (2017)
12. Rangel, J.M.G., Gonçalves, G.R., Pérez, J.A.: The impact of number and spatial distribution of GCPs on the positional accuracy of geospatial products derived from low-cost UASs. Int. J. Remote Sens. **39**, 7154–7171 (2018)
13. Sanz-Ablanedo, E., Chandler, J.H., Rodríguez-Pérez, J.R., Ordóñez, C.: Accuracy of Unmanned Aerial Vehicle (UAV) and SfM photogrammetry survey as a function of the number and location of ground control points used. Remote Sens. **10**, 1606 (2018)
14. Caradonna, G., Tarantino, E., Scaioni, M., Figorito, B.: Multi-image 3D reconstruction: a photogrammetric and structure from motion comparative analysis. In: Gervasi, O., et al. (eds.) ICCSA 2018. LNCS, vol. 10964, pp. 305–316. Springer, Cham (2018). https://doi.org/10.1007/978-3-319-95174-4_25